

Non-intrusive reduced order modelling of multi-fluid flows in oil reservoirs with uncertain rock properties

D. Xiao^{*1}, F. Fang¹, P. Salinas¹, C.C. Pain¹, I.M. Navon², and A. Muggeridge¹

¹Applied Modelling and Computation Group,, Department of Earth Science and Engineering,Imperial College London,, Prince Consort Road, London, SW7 2BP, UK.URL:

<http://amcg.ese.imperial.ac.uk>

²Department of Scientific Computing, Florida State University,Tallahassee, FL, 32306-4120, USA

June 1, 2018

Abstract

A novel variable-material non-intrusive reduced order model (NIROM) based on a Smolyak sparse grid interpolation method, a radial basis function (RBF) method and proper orthogonal decomposition (POD) has been developed for oil reservoirs with uncertain rock properties. This novel NIROM is constructed by using a two level interpolation method. The first level interpolation is constructed for the rock properties, and the second level is for the fluid dynamics. The NIROM is independent of governing equations, therefore, this method is easy to implement and easy to be extended for other applications as it does not require modifications to the source code. The novelty of this work is the use of the presented Smolyak grid and RBF interpolation based NIROM for oil reservoirs with uncertain rock properties. Another novelty is the use of Smolyak sparse grid to reduce the N_R realisations of the reservoir simulator for constructing the NIROM and reduce the computational effort involved in creating the hyperspace of basis functions and coefficients from the snapshots of all the different realisations.

The capability of this new NIROM has been numerically illustrated in two multiphase flows in porous media: a reservoir with eight baffles case and a 3D fluvial channel case with 22 uncertainties. By comparing the results of the novel NIROM against the solutions obtained from the high fidelity full model, it is shown that this model can result in a large reduction in the CPU cost (by a factor of about three orders) while much of the details of multiphase flow in porous media are captured.

^{*}Corresponding author: dh.xiao@imperial.ac.uk

1 Introduction

Production optimisation and history matching are two applications that require the engineer to run numerous flow simulations of flow in the subsurface. Each flow simulation can be very computationally intensive, especially if a reservoir is geologically complex. In some cases it may not be feasible to perform the optimisation sufficiently quickly for it to be useful. This has driven the development of proxy reduced order modelling (ROM) techniques.

Reduced order modelling techniques are distinct from proxy modelling (or neural networks) in that they work by projecting the solutions into a different lower dimensional solution space. In contrast proxy models assume a simple mathematical relationship between the inputs and the outputs of a model of a physical system. The advantages of the reduced order modelling approach are that it can be used to interpret the physical reasons behind an observed behavior and also that, in principal, it can provide a measure of the error in the ROM solution compared with that obtained from the full physics model from which it was generated. ROM techniques have been widely used in various research fields including fluid dynamics ([1, 2]), molecular dynamics ([3]), heat transfer ([4]), data assimilation ([5, 6]), elasticity problems ([7]), shape optimization ([8]), sensor optimization ([9]) and aeroplane components design ([10]) and are becoming more widely discussed in the petroleum engineering literature [11, 12, 13, 14, 15].

Most ROMs have to be hard-coded into the flow simulator (they are intrusive). This means they cannot be used with the commercial simulators that are used by most oil companies. A further problem is that most are derived using POD and/or Galerkin methods. These approaches tend to suffer from non-linear inefficiency and instability issues ([16, 17, 18, 19, 20, 21, 22, 23, 24, 25, 26, 27]).

In order to avoid these issues, the non-intrusive reduced order model (NIROM) has been introduced. Xiao *et al* presented a number of different NIROMs based on a Taylor series based expansion, a Smolyak sparse grid, radial basis functions (RBF) and deep learning ([28, 29, 30, 31]). Lin *et al* presented a NIROM based on least squares fitting and a sparse grid [32]. They have applied this RBF based NIROM to the modelling of inertial flows, multiphase porous media problems, ocean problems as well as to a fluid and solid interaction problem ([33, 34, 33, 35]). Vasile and Winter proposed a non-intrusive approach based on POD and a RBF neural network ([36, 37]). Han proposed a Black Box Stencil interpolation non-intrusive method, and applied it to a 1-D chemical reaction problem and 2-D porous media flow problems ([38]). Raisee *et.al.* have presented a non-intrusive method for the polynomial chaos representation using POD ([39]).

A number of reduced order methods have also been developed for modelling waterflooding in oil reservoirs. Klie proposed a ROM based on the POD, RBF neural network and Discrete Empirical Interpolation Method (DEIM) and used it to predict the production of oil and gas reservoirs ([40]). Cardoso *et al* applied the POD and the trajectory piecewise linear (TPWL) method to model reduction for application to oil production optimization ([11, 12]). The work illustrated the different setting of the injector and the producer wells. Heijn derived a reduced reservoir model through system-theoretical concepts ([13]). He applied the POD-TPWL method into history matching of oil and water systems for production optimization ([14]). Insuasty *et al* presented a tensor based

method for production optimization ([41]). However, geologically heterogeneous reservoirs with varying structures were not discussed. In the work of xiao *et al* [42], a NIROM was applied to multiphase porous media problems, but again was not applied to problems in which the permeability distribution was uncertain. This work firstly used Smolyak sparse grid, RBF and POD based parameterized NIROM for oil reservoirs with uncertain rock properties.

In this paper we outline a non-intrusive ROM that can be used to evaluate waterflooding performance in geologically heterogeneous reservoirs in which the permeability of the different structures (e.g. faults) or deposits (e.g. channels in a fluvial system) are uncertain. This has been implemented using an unstructured mesh finite element porous media flow model ([43]) as the underlying full physics model. The NIROM is demonstrated using a synthetic geological model in which the permeability of the heterogeneities is uncertain: a 2D model of a reservoir with 8 partially communicating faults and a 3D fluvial channel with 3 and 22 uncertainties. The results compare well with those from the full physics model and reduce the CPU time by a factor of a thousand.

The structure of the paper is as follows: Section 2 describes the general problem statement; Section 3 derives the NIROM method using Smolyak sparse grid, RBF and POD method for variable rock properties multiphase flows in porous media; Section 4 illustrates the methodology derived by means of two numerical examples: eight rock layers with different permeabilities and a 3D fluvial channel case are resolved. Finally in Section 5, the conclusion is presented.

2 General Problem Statement

The aim is to create a fast but approximate model that can be used to estimate the spatial distributions of water saturation and pressure, at different times, during the waterflooding of geologically heterogeneous oil reservoirs in which the pattern of permeability is known (e.g. the locations of faults or the facies) but the values of permeability within each element of the pattern are uncertain. We assume that the locations of injection and production wells are fixed and their flow rates are constant and known. A full physics numerical simulator is used to create a number of training data sets. These take the form of a series of snapshots formed of maps of water saturation and pressure at different, equally spaced time instances for specified inputs to the reservoir simulator. These maps of saturation and pressures are described on a fixed mesh. The mesh itself does not have to be structured or uniform but it does not change in time. The steps to create and use the NIROM is thus as follows:

1. the engineer describes the expected pattern of permeabilities within the reservoir of interest;
2. the engineer chooses the range of permeability values that are possible within each region of the pattern. It is assumed that each permeability value within the range is equally probable;
3. N_R realisations of the reservoir are created using a Smolyak sparse grid approach or by random sampling. This specifies the permeability of each region to be used in a given realisation, taken from the range specified in step 2;

4. run the full physics simulator for each of the permeability realisations, k_i , outputting snapshots of the total velocity, pressure and water saturation distribution at N_t equally spaced time intervals covering the full range of times of interest to the engineer. The output times of these snapshots are the same for each simulation;
5. Create the NIROM:
When the engineer wants to use this NIROM to estimate the spatial distribution of the properties of interest (total velocity, water saturation, pressure) at a particular time for a different realisation of permeabilities, an interpolation is performed to estimate the pressure, water saturation and total velocity fields at this time for the new realisation. This means that the computer time taken to estimate the reservoir behaviour for each new realisation is simply the time taken to perform this interpolation. The creation of the NIROM and the interpolation are described in Section 3.

2.1 Full Physics Formulation

Darcy's law for immiscible multiphase flow in porous media has the form:

$$\mathbf{q}_\alpha = -\frac{\mathcal{K}_{r_\alpha}}{\mu_\alpha} \mathbf{K} (\nabla p_\alpha - \mathbf{s}_{u_\alpha}), \quad (1)$$

where \mathbf{q}_α is the α^{th} phase Darcy velocity. The \mathcal{K}_{r_α} is the relative permeability of the α^{th} phase, and it is a function that is denoted by $\mathcal{K}_{r_\alpha}(S_\alpha)$ corresponding to the phase saturation variable S_α . p_α is the pressure of the α^{th} phase. \mathbf{K} is the absolute permeability tensor of the porous medium. μ_α and \mathbf{s}_{u_α} are the phase dynamic viscosity and source term respectively. In this work the fluids are considered incompressible and no source terms are considered, i.e. no gravity or capillary effects are considered.

The saturation equation can be written as:

$$\phi \frac{\partial S_\alpha}{\partial t} + \nabla \cdot (\mathbf{v}_\alpha S_\alpha) = s_{cty,\alpha}, \quad (2)$$

where ϕ denotes the porosity. The t is time and $s_{cty,\alpha}$ is a source term of the α^{th} phase. Finally, equation (2) is bounded by the constraint:

$$\sum_{\alpha=1}^{N_\alpha} S_\alpha = 1, \quad (3)$$

where N_α denotes the number of phases. For more details, see [43, 44, 45].

IC-FERST (Imperial College Finite Element Reservoir SimulaTor) is used here for the forward simulations. However, the creation and use of NIROM is independent of the forward simulator used. In this paper, the spatial discretisation considered is the commonly used Control Volume Finite Element method ([46, 47, 48, 49, 43, 50]). Velocity and pressure are discretised using finite elements, while the saturation is discretised using control volumes to ensure mass conservation. The element pair used in the numerical simulations is the P_1DGP_1 . The velocity is represented using linear discontinuous Galerkin shape functions and pressure is discretised using linear continuous Galerkin

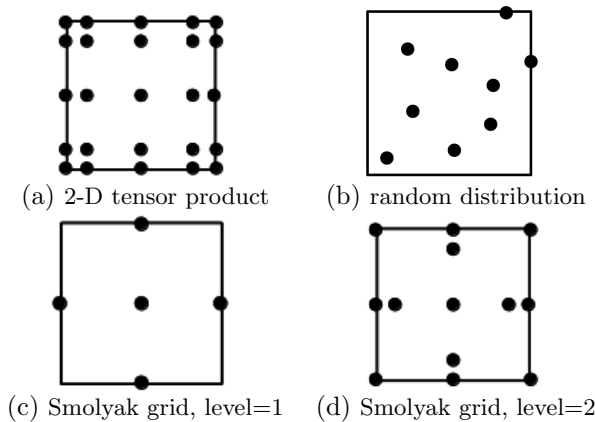


Figure 1: The figures displayed above shows the full tensor product grid, random distribution points and 2-D Smolyak sparse grid with level 1 and 2.

shape functions. Saturation is discretised using control volumes. To discretise time, a Θ -method is used, Θ varies between 1 (backward Euler) and 0.5 (Crank-Nicholson) based on a total variation diminishing (TVD) criterion. Therefore, the time discretisation is always implicit. The non-linear solver used is a modified version of the Anderson solver detailed in [51].

2.2 Creation of the Realisations

The realisations to be used to create the NIROM can be chosen either using a Smolyak grid approach or via random sampling using a radial basis function. These are illustrated schematically in Figure 1 for a system with two regions of different permeability. The Smolyak sparse grid approach results in samples that are spaced on orthogonal grid (1(c) and (d)) whereas the RBF approach (1(b)) results in scattered sample. When interpolating, we need to obtain the values of a function at some points on a grid. A 2D tensor product grid is a set of points distributed regularly on a grid (1(a)), and has the number of C^m , where C denotes the number of points at one dimension, and m is the number of dimension. If the dimension size is high, the number of points can be very huge (curse of dimensionality). This curse of dimensionality motivated the search for a sparse grid. Sergey Smolyak presented a sparse grid ([52]), which selects a relatively small number of nodes on the tensor-product grid. In this case, the values of a function at only a small number of nodes are required, rather than all the nodes on the tensor product grid.

3 Derivation of the NIROM

As discussed in the previous section, the NIROM is created from the snapshots of water saturation and pressure distributions produced by the full physics simulator for each realisation. The workflow to create the NIROM includes two main steps:

1. Determine N_R sets of basis functions, one set for each realisation. Each

set is generated from the N_t snapshots of water saturation and pressure of that realisation using Proper Orthogonal Decomposition (POD);

2. A hypersurface describing the POD basis functions and POD coefficients over all possible permeability values with the specified ranges is created by interpolation using either RBF or the Smolyak sparse grid method;

Once the set of hypersurfaces has been created, the NIROM can then be used to estimate the saturation and pressure distributions that would be obtained for any permeability values within the chosen ranges. Both of Smolyak sparse grid interpolation and RBF interpolation are very close to the full model. The advantage of the Smolyak sparse grid interpolation is the ability to tackle the issue of curse of dimensionality, which can be adopted to reduce the number of training realisations. The details of the above workflow are described below:

3.1 Construction of basis function

A set of basis functions are obtained by the POD method. The POD method projects the solutions from a large system onto a smaller number of orthogonal basis functions. These basis functions are then combined linearly to represent any variables in the large system, which has the form of,

$$\psi = \bar{\psi} + \sum_{i=1}^m \alpha_i \Phi_i, \quad (4)$$

where ψ denotes any variables of interest (*e.g.* the saturation, pressure and density distributions as a function of time), $\bar{\psi}$ is the mean of the variable over the simulation time period, α denotes the POD coefficients, Φ denotes the POD basis functions and m is the number of POD basis functions. The process of obtaining basis functions can be expressed as follows,

- (1) calculate solutions of the full physics system at time levels $1, \dots, N_t$;
- (2) Retrieve a snapshot matrix A from the solutions at all time levels at one realisation;
- (3) Subtract the mean of snapshot matrix A , *i.e.* $A' = A - A_{mean}$;
- (4) Perform Singular Value Decomposition (SVD) on the snapshots matrix A' , *i.e.* $A' = E\Sigma F^T$, where E and F contain the left singular vectors and right singular vectors of A ;
- (5) Choose the number of basis functions, m ($m < N_t$);
- (6) Obtain the POD basis functions $\Phi_i = E_{:,i}$, for $i \in \{1, 2 \dots m\}$;

The POD basis functions at the new unseen rock property point can be obtained by either Smolyak sparse grid interpolation method or RBF interpolation method. The procedure of obtaining the POD basis functions is similar to that of POD coefficients as described in section 3.2.1 and 3.2. If sparse grid interpolation method is chosen, the function values (f) in 20 are values of POD basis functions. If the RBF interpolation method is chosen, the function values ($y_{i,j}$) in 10 are replaced by values of POD basis functions.

3.2 Interpolation of POD basis functions and POD coefficients between realisations

The POD basis functions and POD coefficients interpolation can be constructed either by RBF interpolation or Smolyak sparse grid interpolation methods. The distribution of model parameters can be scatter if we use RBF method. For the Smolyak sparse grid interpolation method, the distribution of model parameters must be regular.

3.2.1 Smolyak sparse grid interpolation method

The Smolyak sparse grid was firstly developed by the mathematician Sergey Smolyak to integrate or interpolate functions with high dimensionality ([52]). The Smolyak sparse grid interpolation is an efficient method that is used to solve high dimensional linear tensor product problems.

One issue with the tensor product approximation is that it requires $O_{l_1} \times \dots \times O_{l_d}$ ($O_{l_1}, O_{l_2}, \dots, O_{l_d}$ are number of knots used in each dimension respectively) values of the function f on a grid. This increases exponentially with the number of dimensions d . This means we need to run full physical simulator for $O_{l_1} \times \dots \times O_{l_d}$ ($O_{l_1}, O_{l_2}, \dots, O_{l_d}$ times), which is too time intensive.

The Smolyak sparse grid method can be used to resolve this 'curse of dimensionality' problem by choosing some of the nodes from the full tensor grid, thus resulting in smaller number of running of full reservoir simulator.

In comparison to tensor product evaluations, computational efficiency is improved, as the number of points no longer increases exponentially with the dimensional size d , for more details, see [28].

The procedure of constructing a set of Smolyak sparse grid interpolation functions for rock properties can be found in Appendix A.

3.2.2 Radial basis functions interpolation

The radial basis function interpolation method can also be used to construct a set of surfaces representing the permeability space. The radial basis function interpolation method is an efficient method to approximate a function using a number of scattered data points. The radial basis functions interpolation method constructs functional approximations in the form of

$$H(\mathbf{k}) = \sum_{i=1}^N w_i \phi(\|\mathbf{k} - \mathbf{k}_i\|), \quad (5)$$

where the interpolation function $H(\mathbf{k})$ is represented as a linear combination of N radial basis functions (ϕ). Each RBF is associated with a different center \mathbf{k}_i (other points), and weighted by a coefficient w_i . $\|\mathbf{k} - \mathbf{k}_i\|$ is a scalar distance r defined by the L_2 norm.

In the RBF interpolation problem, the weight coefficients w_i are determined by ensuring that the interpolation function values $H(\mathbf{k})$ matches the given data y (basis functions) exactly. This is achieved by enforcing $H(\mathbf{k}) = y$, which produces a linear equation

$$Aw = y, \quad (6)$$

where

$$A = \begin{bmatrix} \phi(\|k_1 - k_1\|_2) & \phi(\|k_1 - k_2\|_2) & \cdots & \phi(\|k_1 - k_n\|_2) \\ \phi(\|k_2 - k_1\|_2) & \phi(\|k_2 - k_2\|_2) & \cdots & \phi(\|k_2 - k_n\|_2) \\ \vdots & \vdots & \ddots & \vdots \\ \phi(\|k_n - k_1\|_2) & \phi(\|k_n - k_2\|_2) & \cdots & \phi(\|k_n - k_n\|_2) \end{bmatrix}, \quad (7)$$

$$w = [w_1, w_2, \dots, w_n]^T, y = [y_1, y_2, \dots, y_n]^T \quad (8)$$

The weight coefficients w_j are then determined by solving the linear system (6). y are the values of interpolation function. When we do interpolation of POD coefficients, the y are values of POD coefficients. When we do interpolation of POD basis functions, the y are values of POD basis functions. The process of constructing a set of surfaces for the parameter space can be summarised as Figure 2,

In the Figure 2, a set of surfaces ($H_{\mathbf{u},j}, H_{p,j}, H_{S,j}$) can be obtained by

$$H_j(\mathbf{k}) = \sum_{i=1}^G w_{i,j} \phi_j(\|\mathbf{k} - \mathbf{k}_i\|), \quad (9)$$

where weights $w_{i,j}$ can be calculated by,

$$A_j w_{i,j} = y_{i,j} \quad i \in \{1, 2, \dots, N\}, \quad (10)$$

After obtaining the NIROM, the current POD coefficients can be calculated by,

$$H_j(k_k) = \sum_{i=1}^G w_{i,j} \phi_j(\|(k_k) - (k_j)\|). \quad (11)$$

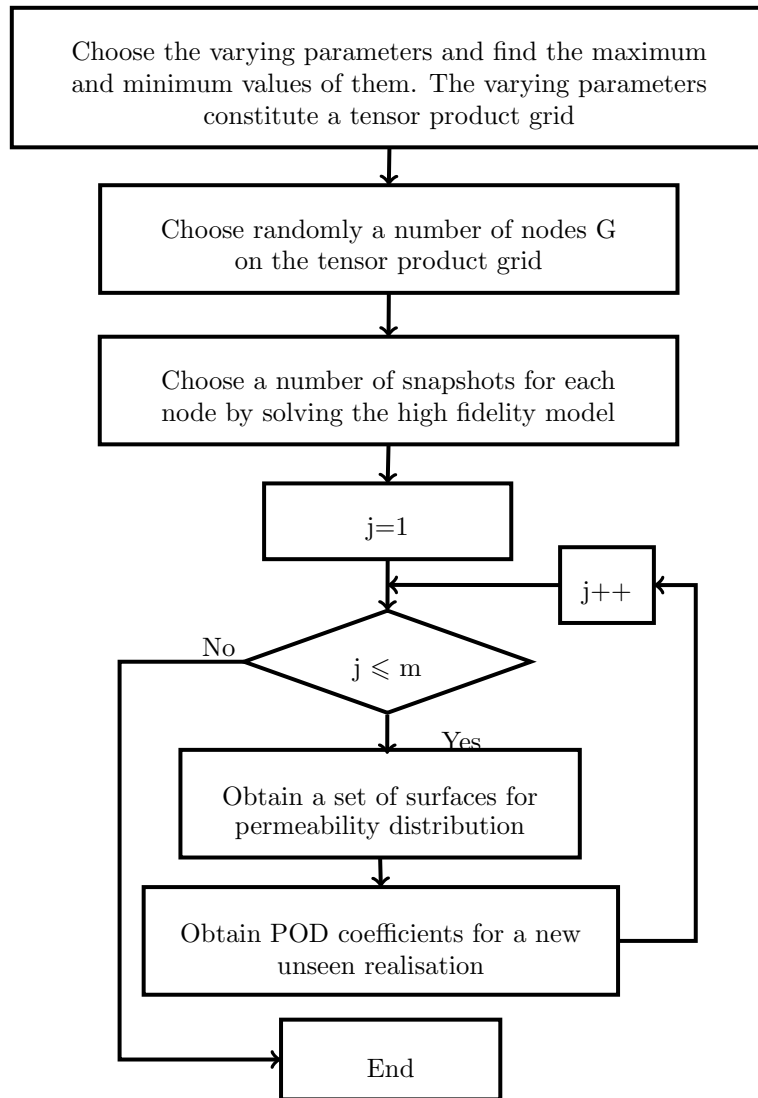


Figure 2: Constructing a set of surfaces for permeability distribution space based on RBF interpolation. m is the number of POD coefficients or POD basis functions. j is the loop variable.

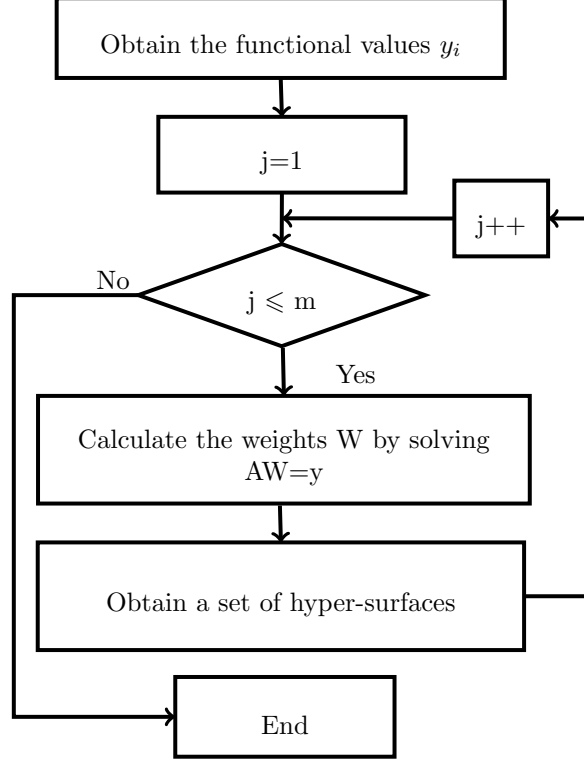


Figure 3: Constructing a set of hypersurfaces for reduced fluid dynamics based on RBF interpolation

3.3 Calculation using the NIROM

The calculation using the NIROM includes offline and online procedures. The offline procedure includes the procedure of constructing fluid dynamics hyper-surfaces based on RBF.

3.3.1 offline: constructing fluid dynamics hyper-surfaces based on RBF

In this section, the process of constructing the second level interpolation functions representing the reduced fluid dynamics system using RBF method is described. The set of hyper-surfaces representing the reduced fluid dynamics are obtained according the Figure 3 below.

In Figure 3, functional value y_i is the variable of interest (pressure saturation etc) at the data point $\boldsymbol{\alpha}^t = (\alpha_u^t, \alpha_p^t, \alpha_s^t)$ from the solutions from the high fidelity model at time level t ($t \in \{1, 2, \dots, N_t\}$), and it equals to α_i^{t+1} .

The equation $AW = y$ has the form of:

$$\begin{bmatrix} \phi(\|\alpha_1 - \alpha_1\|_2) & \phi(\|\alpha_1 - \alpha_2\|_2) & \cdots \phi(\|\alpha_1 - \alpha_{N_t}\|_2) \\ \phi(\|\alpha_2 - \alpha_1\|_2) & \phi(\|\alpha_2 - \alpha_2\|_2) & \cdots \phi(\|\alpha_2 - \alpha_{N_t}\|_2) \\ \vdots & \vdots & \vdots \\ \phi(\|\alpha_{N_t} - \alpha_1\|_2) & \phi(\|\alpha_{N_t} - \alpha_2\|_2) & \cdots \phi(\|\alpha_{N_t} - \alpha_{N_t}\|_2) \end{bmatrix} \begin{pmatrix} w_1 \\ w_2 \\ \vdots \\ w_{N_t} \end{pmatrix} = \begin{pmatrix} y_1 \\ y_2 \\ \vdots \\ y_{N_t} \end{pmatrix}$$

A set of hyper-surfaces $(f_{\mathbf{u},j}, f_{p,j}, f_{S,j})$ can be obtained by substituting the weights into following equations,

$$f_{\mathbf{u},j}(\alpha_{\mathbf{u}}, \alpha_p, \alpha_S) = \sum_{i=1}^{N_t} w_{i,j} \phi_j(\|(\alpha_{\mathbf{u}}, \alpha_p, \alpha_S) - (\alpha_{\mathbf{u}}^i, \alpha_p^i, \alpha_S^i)\|), \quad (12)$$

$$f_{p,j}(\alpha_{\mathbf{u}}, \alpha_p, \alpha_S) = \sum_{i=1}^{N_t} w_{i,j} \phi_j(\|(\alpha_{\mathbf{u}}, \alpha_p, \alpha_S) - (\alpha_{\mathbf{u}}^i, \alpha_p^i, \alpha_S^i)\|), \quad (13)$$

$$f_{S,j}(\alpha_{\mathbf{u}}, \alpha_p, \alpha_S) = \sum_{i=1}^{N_t} w_{i,j} \phi_j(\|(\alpha_{\mathbf{u}}, \alpha_p, \alpha_S) - (\alpha_{\mathbf{u}}^i, \alpha_p^i, \alpha_S^i)\|), \quad (14)$$

3.3.2 Online calculation using NIROM

The online calculation process can be described in Figure 4:

In Figure 4, the initialisation is achieved by treating $\alpha_{\mathbf{u},j}^0$, $\alpha_{p,j}^0$ and $\alpha_{S,j}^0$ as the initial values. The solutions at current time level n can be obtained by assigning a complete set of POD coefficients $\alpha_{\mathbf{u},j}^{n-1}$, $\alpha_{p,j}^{n-1}$ and $\alpha_{S,j}^{n-1}$ at previous time level $n-1$ into the hyper-surface $f = (f_{\mathbf{u},j}, f_{p,j}, f_{S,j})$:

$$f_{\mathbf{u},j} \leftarrow (\alpha_{\mathbf{u}}^{n-1}, \alpha_p^{n-1}, \alpha_S^{n-1}), \quad f_{p,j} \leftarrow (\alpha_{\mathbf{u}}^{n-1}, \alpha_p^{n-1}, \alpha_S^{n-1}), \quad f_{S,j} \leftarrow (\alpha_{\mathbf{u}}^{n-1}, \alpha_p^{n-1}, \alpha_S^{n-1}). \quad (15)$$

Then, the POD coefficients of the current time level are,

$$\alpha_{\mathbf{u},j}^n = f_{\mathbf{u},j} = \sum_{i=1}^{N_t} w_{i,j} \phi_{i,j}(r), \quad \alpha_{p,j}^n = f_{p,j} = \sum_{i=1}^{N_t} w_{i,j} \phi_{i,j}(r), \quad \alpha_{S,j}^n = f_{S,j} = \sum_{i=1}^{N_t} w_{i,j} \phi_{i,j}(r), \quad (16)$$

where, $r = \|(\alpha_{\mathbf{u}}, \alpha_p, \alpha_S) - (\alpha_{\mathbf{u}}^i, \alpha_p^i, \alpha_S^i)\|$.

After obtaining the POD coefficients, the solutions of the NIROM can be obtained by projecting $\alpha_{\mathbf{u},j}^n$, $\alpha_{p,j}^n$ and $\alpha_{S,j}^n$ onto the full space using the equations,

$$\mathbf{u}^n = \sum_{j=1}^m \alpha_{\mathbf{u},j}^n \Phi_{\mathbf{u},j}, \quad p^n = \sum_{j=1}^m \alpha_{p,j}^n \Phi_{p,j}, \quad S^n = \sum_{j=1}^m \alpha_{S,j}^n \Phi_{S,j}. \quad (17)$$

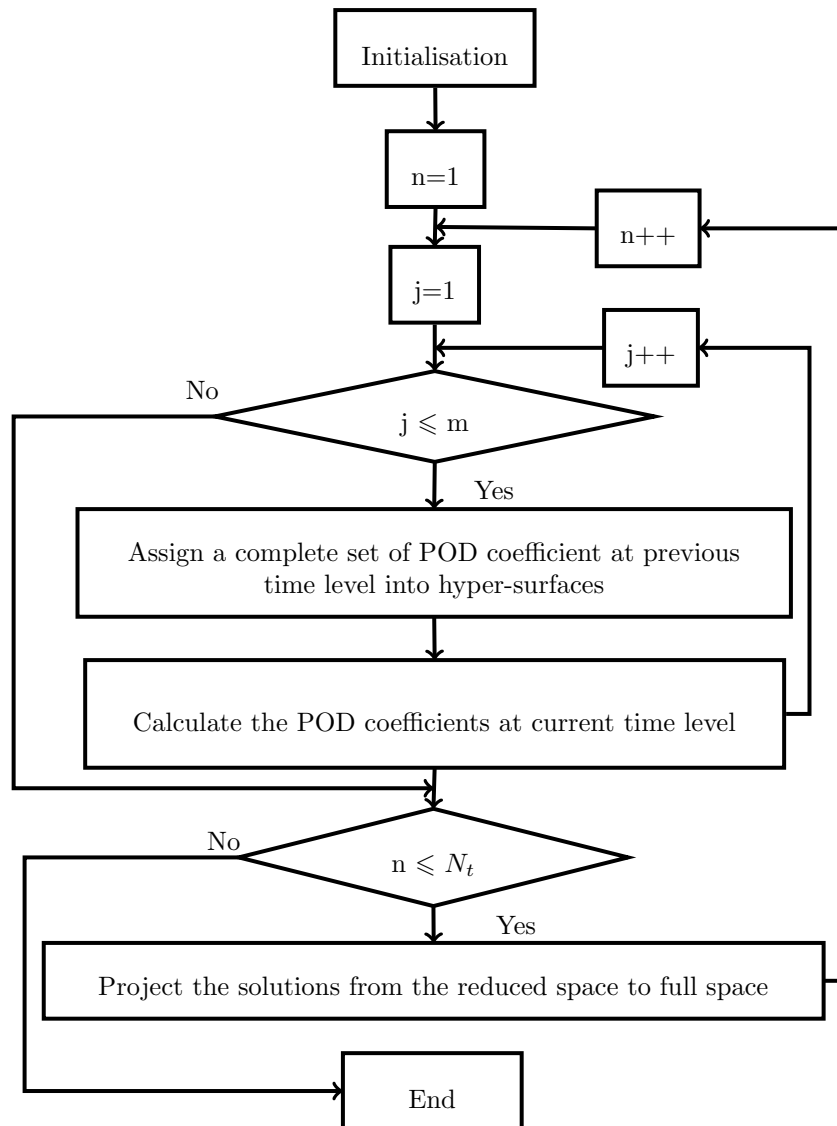


Figure 4: Online calculation procedure using NIROM

4 Application of the NIROM

In this section full models are run with the reservoir simulator IC-FERST (Imperial College Finite Element Reservoir Simulator). IC-FERST is a multiphase porous media flow simulator, based on surface based modelling, which includes: high order time and space discretization, discontinuous and or control volume pressure representation, unstructured dynamic mesh optimization and ability to solve for high Courant numbers ([43, 44, 53, 54, 55]).

During the simulation, a number of full physics simulations are run first. The number of runs is dependent of the number of nodes in the Smolyak sparse grid. The NIROM then is created from snapshots obtained from a full physics simulation of the fluid flows of interest. For the second numerical experiment the range of the permeabilities of the different variations is not provided due to the extent of the particular permeability values used, however, a range of values is provided. To calculate the relative permeability values the Brooks-Corey ([56]) model is used:

$$k_{rw}(S_w) = k'_w \left(\frac{S_w - S_{wirr}}{1 - S_{wirr} - S_{nwr}} \right)^{n_w}, \quad (18)$$

$$k_{rnw}(S_w) = k'_{nw} \left(\frac{S_{nw} - S_{nwr}}{1 - S_{wirr} - S_{nwr}} \right)^{n_{nw}}, \quad (19)$$

where k'_w , k'_{nw} , S_{wirr} and S_{nwr} are the endpoint water relative permeability, endpoint oil relative permeability, the immobile fractions of the wetting and non-wetting phase respectively. These properties are defined in Table 1. The mesh sizes have been chosen as a balance between the coarsest mesh able to represent the desired geology and to provide good numerical results in the forward model and in the NIROM. In the first numerical example using a structured mesh and in the second one using an unstructured mesh.

	M^0	$S_{wirr} = S_{nwr}$	$n_w = n_{nw}$	k'_w	k'_{nw}	ϕ	# nodes
4.1	10	0.2	2	1.0	1.0	0.2	2646
4.2	4	0.2	2	0.3	0.8	0.2	31776

Table 1: Model set-up for the test cases 4.1 and 4.2; M^0 is the viscosity contrast between the phases.

4.1 Numerical example 1: reservoir with eight baffles

The first test case is comprised of eight low permeability barriers embedded in a higher permeability domain as illustrated in Figure 5. The domain has a non-dimensional size 10×10 . The permeability of the eight barriers in this test case are between 0.1 and 0.5 dimensionless permeability units, and the permeability of the background is 10 dimensionless permeability units. The full model simulation was run during the simulation period $[0, 5]$ with a time step size of 0.01. 50 snapshots of solutions were collected at regularly spaced time intervals $\Delta t = 0.1$ for each solution variable. The injection was controlled by constant inlet velocity, $v = (1, 1)$, from the lower left corner of the domain, see Figure 5.

In this example, the Smolyak sparse grid has a dimensional size of eight, and there are 17 nodes in the sparse grid in terms of level one. Table 2 lists permeability combinations of the eight-barrier case using level one-labelled E1-E17. An unseen Smolyak sparse node (0.1, 0.5, 0.5, 0.5, 0.1, 0.5, 0.5, 0.5)-labelled P1 is chosen to show the capabilities of the NIROM.

Table 2: Permeability combinations for the eight-barrier test case with level one

Cases \ Barriers	1	2	3	4	5	6	7	8
E1	0.3	0.3	0.3	0.3	0.3	0.3	0.3	0.3
E2	0.1	0.3	0.3	0.3	0.3	0.3	0.3	0.3
E3	0.5	0.3	0.3	0.3	0.3	0.3	0.3	0.3
E4	0.3	0.1	0.3	0.3	0.3	0.3	0.3	0.3
E5	0.3	0.5	0.3	0.3	0.3	0.3	0.3	0.3
E6	0.3	0.3	0.1	0.3	0.3	0.3	0.3	0.3
E7	0.3	0.3	0.5	0.3	0.3	0.3	0.3	0.3
E8	0.3	0.3	0.3	0.1	0.3	0.3	0.3	0.3
E9	0.3	0.3	0.3	0.5	0.3	0.3	0.3	0.3
E10	0.3	0.3	0.3	0.3	0.1	0.3	0.3	0.3
E11	0.3	0.3	0.3	0.3	0.5	0.3	0.3	0.3
E12	0.3	0.3	0.3	0.3	0.3	0.1	0.3	0.3
E13	0.3	0.3	0.3	0.3	0.3	0.5	0.3	0.3
E14	0.3	0.3	0.3	0.3	0.3	0.3	0.1	0.3
E15	0.3	0.3	0.3	0.3	0.3	0.3	0.5	0.3
E16	0.3	0.3	0.3	0.3	0.3	0.3	0.3	0.1
E17	0.3	0.3	0.3	0.3	0.3	0.3	0.3	0.5
P1	0.1	0.5	0.5	0.5	0.1	0.5	0.5	0.5

Figure 6 shows the solutions of saturation from full model and the NIROM with 6, 12 and 24 POD bases at dimensionless time instances 1.5 and 4.0 using smolyak level one. It can be seen that the NIROMs has captured most of the energy. The NIROM with 24 POD bases provides more accurate results, compared with the high fidelity model, than NIROMs with 6 and 12 POD bases. This is also reflected in Figure 7, which shows the error between the full model and NIROM with 6, 12 and 24 POD basis functions at dimensionless time instances 1.5 and 4.0. In the error figures, the errors are between 0 – 0.02. The solutions obtained from the high fidelity model and NIROMs at a particular point in the domain are presented in Figure 8. It again shows that the saturation solutions from NIROMs with 6, 12 and 24 POD bases are close to the high fidelity full model. Again, the NIROM with larger number of POD basis functions provides higher accuracy than that of with the smaller number of POD basis functions. This is confirmed by the inspection of the RMSE and correlation coefficient, shown in Figure 9.

In order to compare the performance of NIROMs using Smolyak sparse grid and RBF, the saturation profile and saturation values comparison at a particular point ($x=1.9048, y=2.381$) are presented in figures 10 and 11, respectively. Figure 10 shows the saturation profile of the high fidelity model, NIROM with Smolyak sparse grid using 24 POD basis functions and NIROM with RBF using 24 POD basis functions. It can be seen that the saturation field provided by NIROM with RBF is better, compared to the full model, than the saturation

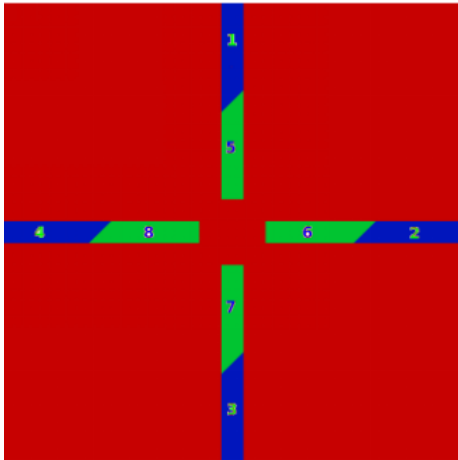


Figure 5: distribution of permeability in the domain, the permeability of the eight barriers are between 0.1 and 0.5; The permeability of the background is 10 dimensionless units of permeability.

profile obtained by using NIROM with Smolyak sparse grid. This can also be seen from Figure 11, where the two NIROMs perform well at the particular point ($x=1.9048$, $y=2.381$). However, NIROM with RBF performs better than NIROM with Smolyak sparse grid. Both methods have the same online and offline CPU cost.

4.2 Numerical example 2: 3D fluvial channel case

The second case examined is a 3D model of a reservoir containing a number of high permeability channels. There are three types of channels in the reservoir and each type has a different permeability and associated uncertainty. The different channel types are shown in different colors: blue, yellow and red. The water is injected into the computational domain from the right side to the left with a pressure gradient of (5.5×10^7 Pa). The simulation was run over the simulation period $[0, 1000 \text{days}]$ with a time step size of 10 days. 20 snapshots of solutions were taken at regularly spaced time intervals $\Delta t = 50$ days for each solution variable (pressure, saturation and velocity).

In this test case, 23 training simulations were used to construct the NIROM with RBF interpolation. In order to test the capability of the NIROM, three new cases with different permeabilities were simulated. In each of the 23 training simulations, the permeabilities of two channels (the blue and the red channels in Figure 12(b)) were modified randomly. The distribution of the 23 simulations with the different permeabilities used is shown in Figure 12 using miliDarcies ($1mD = 9.869233 \times 10^{16}m^2$). The permeabilities were varied between 50 mD and 1000 mD. The three new test simulations are points A, B and C in the Figure 12 (a). Point A is the closest point to the training points, and point B is further away from the training points. Point C is outside the training domain $[50 - 1000]mD$.

Figure 13 shows the saturation obtained from the full model and NIROM after 15 days at point A (460, 360) mD. Figure (c) compares the saturation

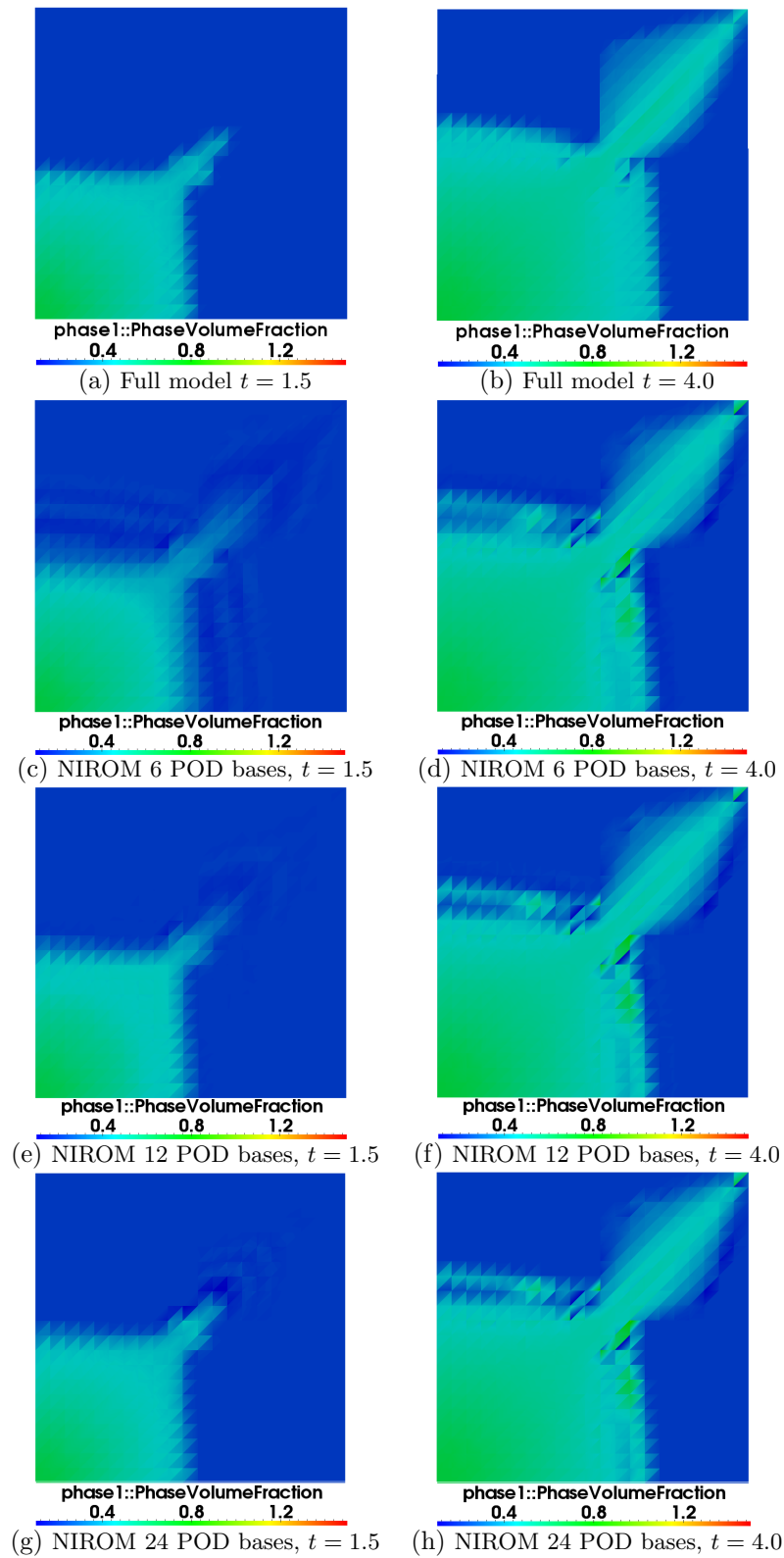


Figure 6: 8 baffles case: the figures displayed above show the solutions of saturation from full model and the NIROM of 6, 12 and 24 POD bases at dimensionless time instances 1.5 and 4.0 using smolyak *level one*.

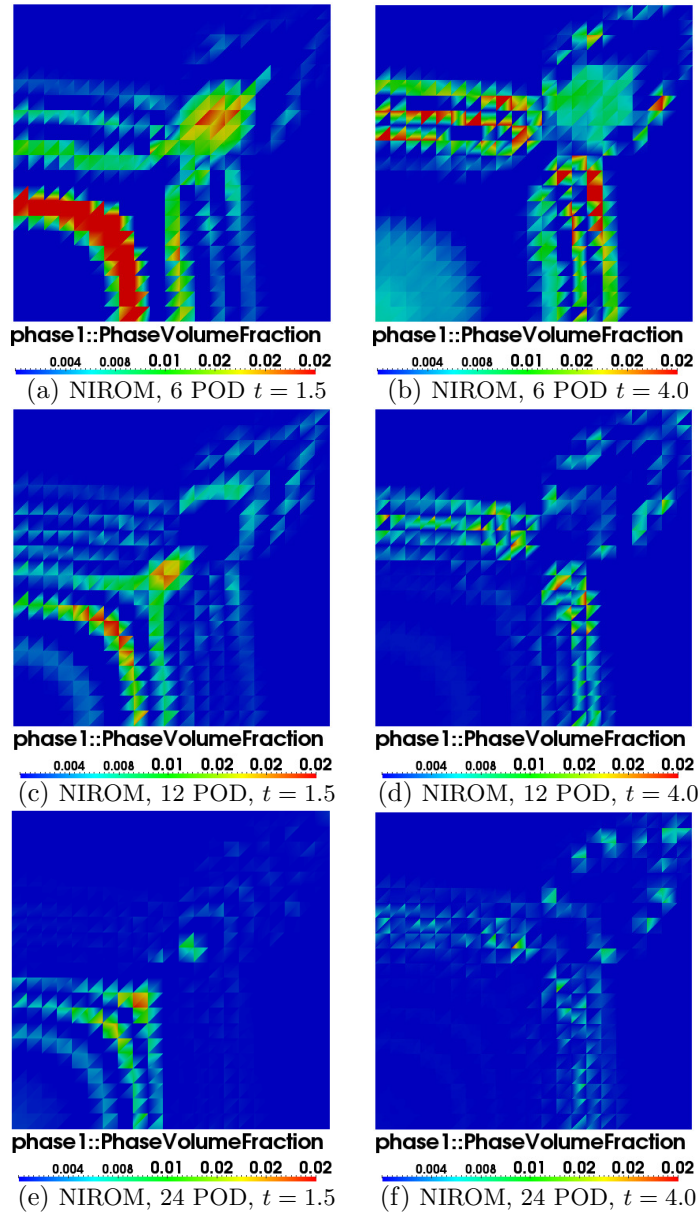


Figure 7: 8 baffles case: the figures displayed above show the error between the full model and the NIROM of 6, 12 and 24 POD bases at dimensionless time instances 1.5 and 4.0.

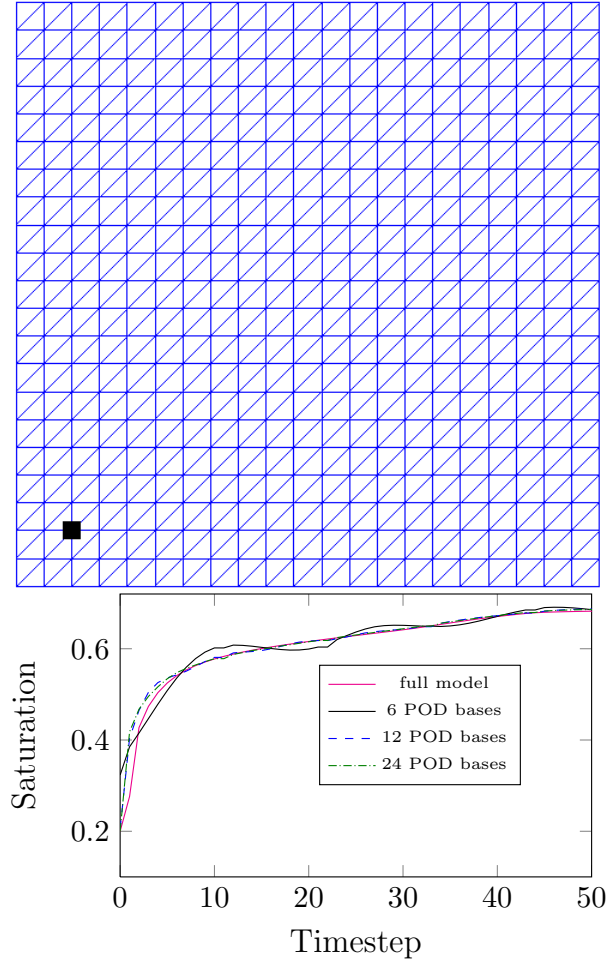


Figure 8: 8 baffles case: the graphs show the saturation solutions predicted by the full model, and the NIROM at position $(0.95238, 0.95238)$.

obtained from two models at a particular location $x = 184.25, y = 110$ in the computational domain, see Figure 12 (b). As can be seen from the figure, the results of the NIROM using permeability values close to those used in the training set better match with the results obtained from the full physics model. Figure 14 shows the saturation profile from the full model and the NIROM at time 25 days at point B $(475, 750)$ mD. The saturation obtained from the two models at a particular location $x = 184.25, y = 110$ in the computational domain, see Figure 12 (b), is given in the sub-figure (c). The NIROM results differ more from the simulation shown at point A. Figure 15 compares the saturation profile of the full model and NIROM after time 30 days at point C $(450, 1250)$ mD. Figure 15 (c) compares the saturation value obtained by the two models at $x = 184.25, y = 110$ in the computational domain. The permeabilities of the widest channel and narrowest channel are $(450, 1250)$ mD, which are outside the domain of the training points. NIROM results are less accurate in this case, as expected.

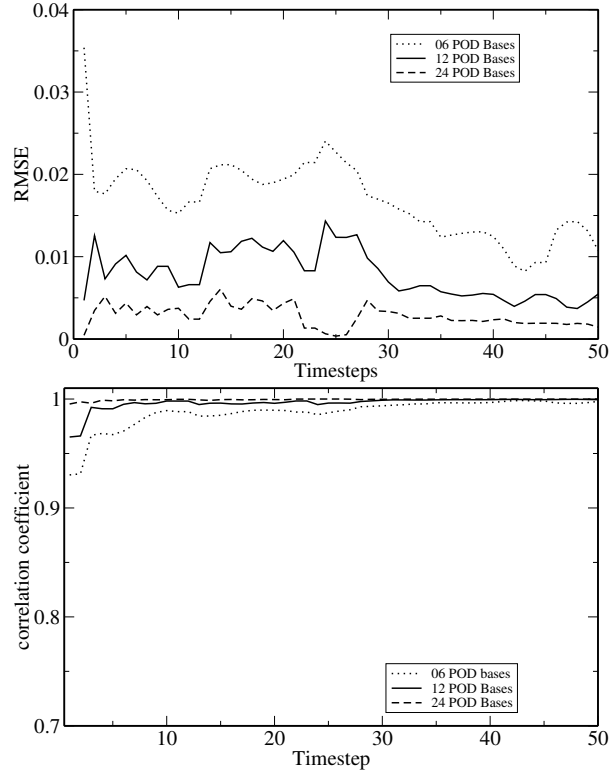


Figure 9: The graph shows the RMSE errors and correlation coefficient calculated for the NIROM model for the 8 layers case.

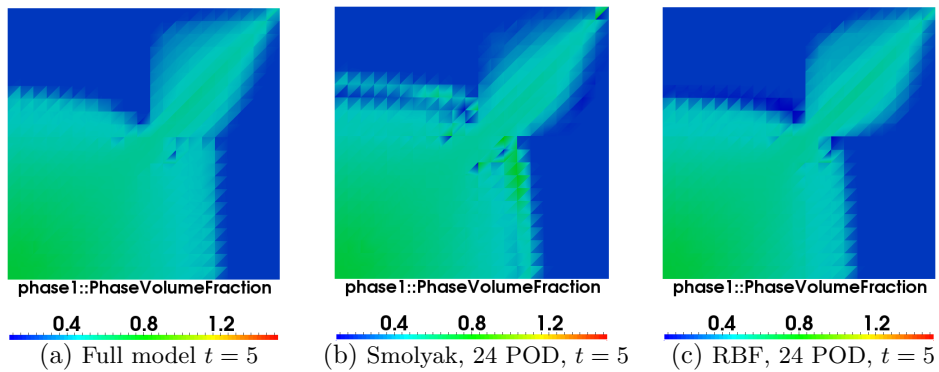


Figure 10: 8 baffles case: saturation comparison between the high fidelity full model, NIROM with Smolyak sparse grid and NIROM with RBF at time level $t = 5$ dimensionless seconds.

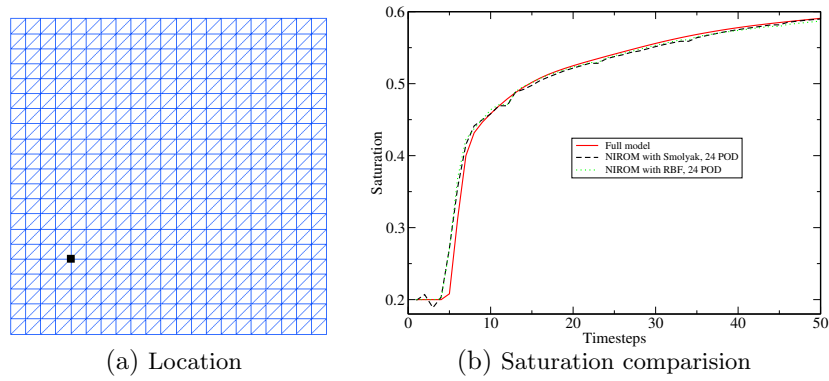


Figure 11: 8 baffles case: saturation values comparison between the full model, NIROM with Smolyak grid and RBF using 24 POD basis functions at a particular point ($x=1.9048$, $y=2.381$) on the domain.

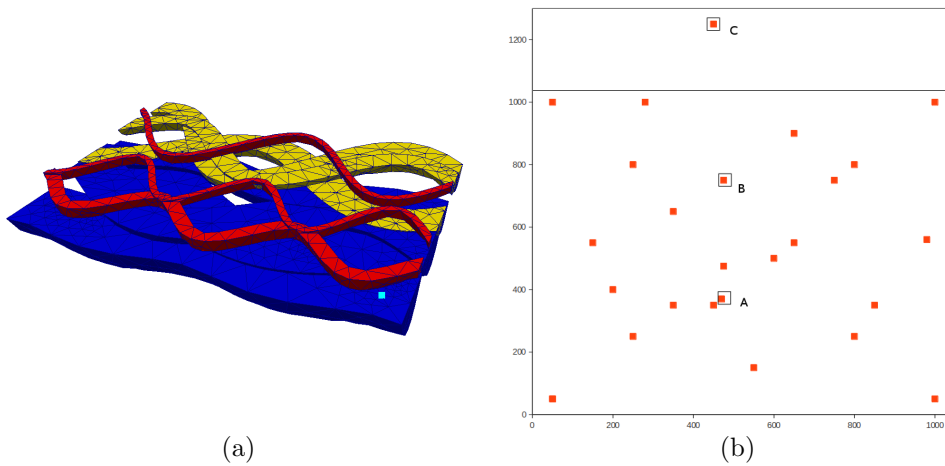


Figure 12: (a) the different channel types: blue (wide channels), yellow (medium width) and red (small channels); (b) the distribution of permeabilities used for the red and blue channels (X-Y axis are in mD). The yellow channels has fixed permeability equal to 200mD.

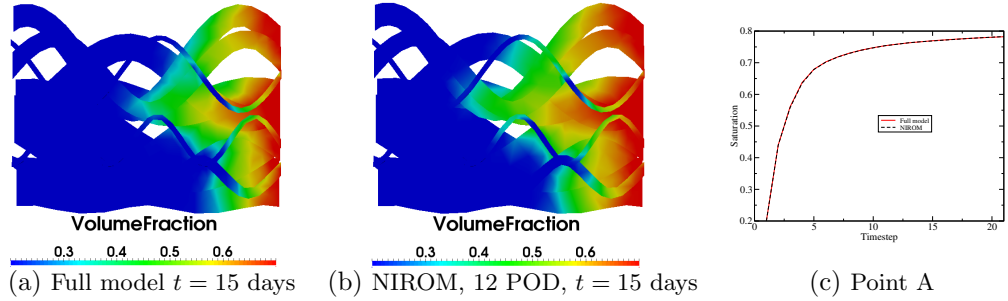


Figure 13: Channel case: the saturation distribution obtained from the full physical model and NIROM with 12 POD basis functions at time level $t = 15$ days for the permeabilities shown at point A (460, 360) in Figure 12 (b). Figure (c) shows a comparison of the saturation value at $x = 184.25, y = 110$ in the computational domain, see the pale blue square in Figure 12 (a).

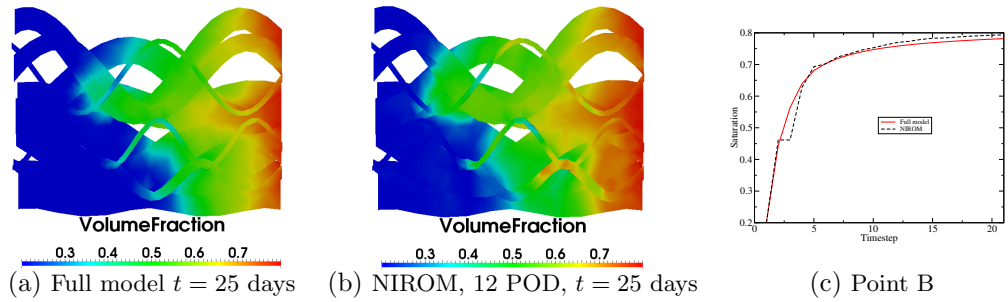


Figure 14: Channel case: the saturation distribution obtained from the full physical model and NIROM with 12 POD basis functions at time level $t = 25$ days at location B in Figure 12 (b).

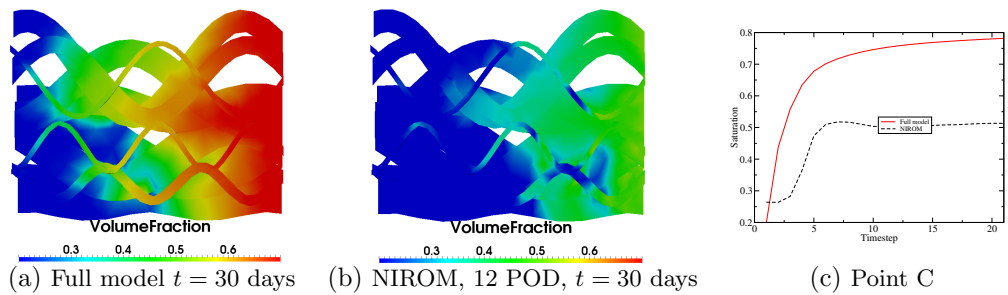


Figure 15: Channel case: the saturation distribution obtained from the full physical model and NIROM with 12 POD basis functions at time level $t = 30$ days at location C in Figure 12 (a).

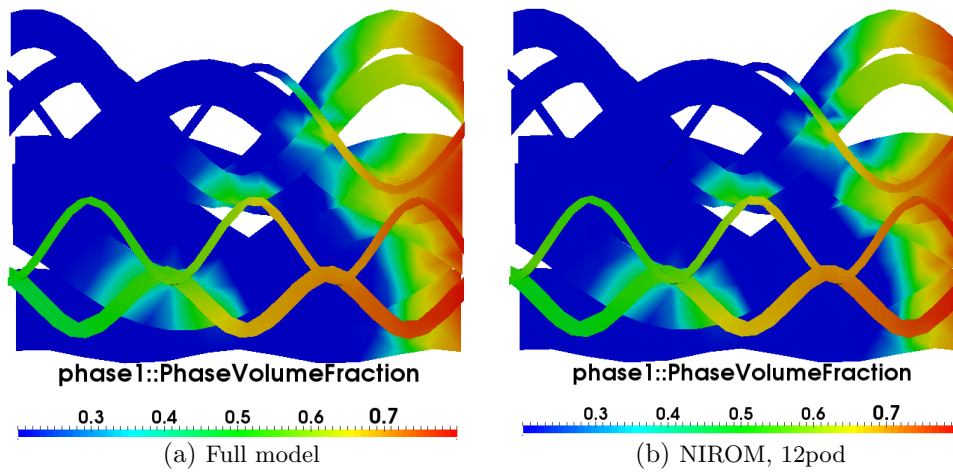


Figure 16: Channel case: Saturation from full model and NIROM with 22 varying input permeabilities.

In order to test the capabilities of the NIROM, The reservoir was divided into 22 types of channels; each channel has a different permeability and associated uncertainty. 49 training simulations were used in this example.

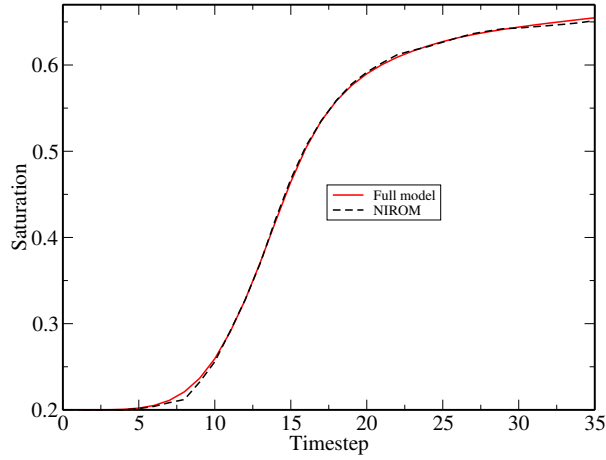


Figure 17: Reservoir with 22 types of channels: the graph shows the saturation comparison between the full model and NIROM at an unseen point based on 49 training simulations particular point ($x=-18.378$, $y=184.25$, $z=110$).

4.3 Computational efficiency

Table 3 shows a comparison of the online CPU time required for running the full model and NIROM. The simulations were performed on 12 cores machine of an Intel® Xeon® X5680 processor with 3.3GHz and 48GB RAM. The test cases were run in serial, which means only one core was used when simulating. It can be seen that the online CPU time required for running the NIROM is considerably less than that for the full model and is reduced by a factor of 2500. It is worth noting that as the number of nodes increases, the CPU time required for the full model also increases, while the CPU time for the NIROM remains almost the same.

The offline CPU time required for constructing the NIROM includes the time of forming the POD bases and interpolation functions. It is found that the time for calculating the interpolation functions can be ignored. The offline CPU time is dependent on the number of nodes in the computational domain and POD bases. The offline CPU time has a linear relationship with the number of POD bases and nodes. The number of nodes used in two examples is not big, so the offline CPU cost is not too much.

Table 3: Comparison of the online CPU time (seconds) required for running the full model and NIROM during one time step.

Cases	Model	Assembling and solving	Projection	Interpolation	Number of POD	Number of nodes	Total
Baffles	Full	1.730	0	0	12	2646	1.731
	NIROM	0	0.0003	0.0001	12	2646	0.00040
Channels	Full	74.9200	0	0	12	31776	74.920
	NIROM	0	0.0003	0.0001	12	31776	0.00040

5 Conclusion

In this article a new non-intrusive reduced order model for multi-fluid flows in oil reservoirs with uncertain rock properties is presented. It was constructed by using a set of surfaces for the rock properties and a set of hyper-surfaces for the fluid dynamics. This NIROM is easy to implement, modify and extend. This model was implemented under the framework of a 3D unstructured mesh multiphase porous media model, Imperial College Finite Element Reservoir Simulator (IC-FERST) and firstly applied to multi-fluid flows in oil reservoirs with uncertain rock properties. The results of numerical examples show that the NIROM solves accurately the multi-fluid flows in oil reservoirs with uncertain rock properties with a high degree of computational efficiency. The errors of the NIROM is analysed by RMSE and correlation coefficient.

Running always full physical systems may be unnecessarily time consuming if exploring a parameter range of a numerical model. In these cases, using NIROM can extraordinarily increase the computational efficiency while providing accurate enough results. In the NIROM, if we choose an unseen set of model parameter outside the training data domain, we would not get satisfactory results, however, we can avoid this by choosing larger training data domain. It would be interesting to apply this approach to commercial software, such as ECLIPSE (reservoir simulator). It would be also interesting to apply this approach to uncertainty quantification and sensitivity analysis.

Acknowledgment

The authors are grateful for the support of the EPSRC grant: Managing Air for Green Inner Cities (MAGIC)(EP/N010221/1), EPSRC MEMPHIS multiphase flow programme grant (EP/K003976/1), NSFC grant 11502241, EPSRC (Smart-GeoWells grant EP/R005761/1), funding from the European Union Seventh Frame work Programme (FP7/20072013) under grant agreement No.603663 for the research project PEARL (Preparing for Extreme And Rare events in coastal regions). Prof. Pain and Pablo would like to thank EXXON for helping to fund the new unstructured mesh model used here; Prof. Pain, Prof. Muggeridge and Fang are grateful for the support of BP Exploration on reduced order modelling under the LAMBSID project.

Appendix A

The procedure of constructing a set of Smolyak sparse grid interpolation functions for rock properties is described as following,

- (1) Determine d rock property variables $\{k_1, k_2, \dots, k_d\}$ where d is the number of varying rock types or permeability regions and calculate the minimum and maximum values of those variables. Each rock property variable constitute a dimension of a Smolyak sparse grid;
- (2) Construct a d dimensional Smolyak sparse grid for the rock property variables;
- (3) Obtain rock property values $\mathbf{k}^i = \{k_1^i, k_2^i, \dots, k_d^i\}, i \in (1, 2, \dots, N_R)$ at each dimension for N_R Smolyak sparse grid nodes;

- (4) Create N_R realisations using different permeability values in the chosen pattern of permeability. Each Smolyak sparse grid node is associated with a full physical simulation;
- (5) Run a full physics simulation and generate a number of snapshots using permeability values at the associated Smolyak sparse grid;
- (6) Save the snapshots of the variables of interest at each time t where $t \in (1, 2, \dots, N_t)$;
- (7) Generate N_R sets of POD basis functions $\{\Phi_{\mathbf{u}}^1, \Phi_p^1, \Phi_S^1\}, \{\Phi_{\mathbf{u}}^2, \Phi_p^2, \Phi_S^2\}, \dots, \{\Phi_{\mathbf{u}}^{N_R}, \Phi_p^{N_R}, \Phi_S^{N_R}\}$ for each Smolyak sparse grid node $k^i, i \in (1, 2, \dots, N_R)$ by performing a truncated SVD of the snapshots matrix obtained from corresponding set of snapshots;
- (8) Obtain a number of basis functions for a new rock property point k^i within the domain of the tensor product grid via the Smolyak sparse grid interpolation method. A tensor product grid has a total number of nodes of O^d where there are O points used in each dimension and d is the size of dimensionality);
- (9) Obtain a set of surfaces by using the Smolyak sparse grid interpolation formulation,

$$\hat{A}(k, d) = \sum_{\max(d, l+1) \leq |\mathbf{l}| \leq d+l} (-1)^{d+l-|\mathbf{l}|} \cdot \binom{d-1}{d+l-|\mathbf{l}|} (U^{l_1} \otimes \dots \otimes U^{l_d}), \quad (20)$$

where $|\mathbf{l}| = l_1 + \dots + l_d$, $(U^l)(f) = \sum_{i=1}^{O^l} f(k_i^l) \cdot (H_i^l(k))$, \hat{A} is the interpolation function, l denotes the grid level, $H_i^l \in C([-1, 1])$ is the approximation formulas and $f(k_i^l)$ denotes the value of the function f at k_i^l .

References

- [1] Yuepeng Wang^a, I Michael Navon^b, Xinyue Wang^c, and Yue Cheng^d. 2D Burgers Equations with Large Reynolds Number Using POD/DEIM and Calibration. *In press, International Journal of Numerical Methods in Fluids*, 2016.
- [2] Manal Alotaibi, Victor M. Calo, Yalchin Efendiev, Juan Galvis, and Mehdi Ghommem. Globallocal nonlinear model reduction for flows in heterogeneous porous media. *Computer Methods in Applied Mechanics and Engineering*, 292:122 – 137, 2015. Special Issue on Advances in Simulations of Subsurface Flow and Transport (Honoring Professor Mary F. Wheeler).
- [3] KC Hoang, Y Fu, and JH Song. An hp-proper orthogonal decomposition–moving least squares approach for molecular dynamics simulation. *Computer Methods in Applied Mechanics and Engineering*, 298:548–575, 2016.
- [4] Benjamin Peherstorfer and Karen Willcox. Data-driven operator inference for nonintrusive projection-based model reduction. *Computer Methods in Applied Mechanics and Engineering*, 306:196 – 215, 2016.
- [5] Gabriel Dimitriu, Narcisa C Apreutesei, and Razvan Stefanescu. Numerical Simulations with Data Assimilation Using an Adaptive POD Procedure. In *LSSC*, pages 165–172. Springer, 2009.
- [6] Gabriel Dimitriu and Narcisa Apreutesei. Comparative study with data assimilation experiments using proper orthogonal decomposition method. In *International Conference on Large-Scale Scientific Computing*, pages 393–400. Springer, 2007.
- [7] K.C. Hoang, P. Kerfriden, and S.P.A. Bordas. A fast, certified and tuning free two-field reduced basis method for the metamodelling of affinely-parametrised elasticity problems. *Computer Methods in Applied Mechanics and Engineering*, 298:121 – 158, 2016.
- [8] Guenael Le Quilliec, Balaji Raghavan, and Piotr Breitkopf. A manifold learning-based reduced order model for springback shape characterization and optimization in sheet metal forming. *Computer Methods in Applied Mechanics and Engineering*, 285:621 – 638, 2015.
- [9] Fangxin Fang, ChristopherC Pain, Ionel Navon, and Dunhui Xiao. An efficient goal based reduced order model approach for targeted adaptive observations. *International Journal for Numerical Methods in Fluids*, 2016.
- [10] Andrea Manzoni, Filippo Salmoiraghi, and Luca Heltai. Reduced basis isogeometric methods (rb-iga) for the real-time simulation of potential flows about parametrized {NACA} airfoils. *Computer Methods in Applied Mechanics and Engineering*, 284:1147 – 1180, 2015. Isogeometric Analysis Special Issue.
- [11] MA Cardoso et al. Reduced-order models for reservoir simulation. In *SPE Annual Technical Conference and Exhibition*, number SPE-129636-STU. Society of Petroleum Engineers, 2009.

- [12] Marco A Cardoso, Louis J Durlofsky, et al. Use of reduced-order modeling procedures for production optimization. *SPE Journal*, *SPE-119057-MS*, 15(02):426–435, 2010.
- [13] T Heijn, R Markovinovic, JD Jansen, et al. Generation of low-order reservoir models using system-theoretical concepts. In *SPE Reservoir Simulation Symposium*, *SPE-79674-MS*. Society of Petroleum Engineers, 2003.
- [14] Jincong He. *Reduced-Order Modeling for Oil-Water and Compositional Systems, with Application to Data Assimilation and Production Optimization*. PhD thesis, Stanford University, 2013.
- [15] Zeid M Alghareeb, John Williams, et al. Optimum decision-making in reservoir management using reduced-order models. In *SPE Annual Technical Conference and Exhibition*, *SPE-166305-MS*. Society of Petroleum Engineers, 2013.
- [16] S Walton, O Hassan, and K Morgan. Reduced order modelling for unsteady fluid flow using proper orthogonal decomposition and radial basis functions. *Applied Mathematical Modelling*, 37(20):8930–8945, 2013.
- [17] Michael Schlegel and Bernd R. Noack. On long-term boundedness of Galerkin models. *Journal of Fluid Mechanics*, 765:325–352, 2 2015.
- [18] Jan Osth, Bernd R. Noack, Sinisa Krajnovic, Diogo Barros, and Jacques Boree. On the need for a nonlinear subscale turbulence term in POD models as exemplified for a high-Reynolds-number flow over an Ahmed body. *Journal of Fluid Mechanics*, 747:518–544, 5 2014.
- [19] S. Chaturantabut and D.C. Sorensen. Nonlinear model reduction via discrete empirical interpolation. *SIAM J. Sci. Comput*, 32:2737–2764, 2010.
- [20] M. Barrault, Y. Maday, N.C. Nguyen, and A.T. Patera. An empirical interpolation method: application to efficient reduced-basis discretization of partial differential equations. *C. R. Acad. Sci. Paris, Ser.*, 339:667–672, 2004.
- [21] D. Xiao, F. Fang, A. G. Buchan, C.C. Pain, I.M. Navon, J. Du, , and G. Hu. Non-linear model reduction for the Navier-Stokes equations using Residual DEIM method. *Journal of Computational Physics*, 263:1–18, 2014.
- [22] Kevin Carlberg, Charbel Farhat, Julien Cortial, and David Amsallem. The GNAT method for nonlinear model reduction: effective implementation and application to computational fluid dynamics and turbulent flows. *Journal of Computational Physics*, 242:623–647, 2013.
- [23] Kevin Carlberg, Charbel Bou-Mosleh, and Charbel Farhat. Efficient nonlinear model reduction via a least-squares petrov–galerkin projection and compressive tensor approximations. *International Journal for Numerical Methods in Engineering*, 86(2):155–181, 2011.
- [24] Yunfei Chu, Mitchell Serpas, and Juergen Hahn. State-preserving nonlinear model reduction procedure. *Chemical engineering science*, 66(17):3907–3913, 2011.

- [25] Karen Willcox and Alexandre Megretski. Model reduction for large-scale linear applications. In *Proc. of 13th IFAC Symposium on System Identification, Rotterdam, Netherlands*, pages 1431–1436, 2003.
- [26] Feriedoun Sabetghadam and Alireza Jafarpour. α Regularization of the POD-Galerkin dynamical systems of the KuramotoSivashinsky equation. *Applied Mathematics and Computation*, 218(10):6012 – 6026, 2012.
- [27] D. Xiao, F. Fang, J. Du, C.C. Pain, I.M. Navon, A. G. Buchan, A.H. ElSheikh, and G. Hu. Non-linear Petrov-Galerkin methods for reduced order modelling of the Navier-Stokes equations using a mixed finite element pair. *Computer Methods In Applied Mechanics and Engineering*, 255:147–157, 2013.
- [28] D. Xiao, F. Fang, A.G. Buchan, C.C. Pain, I.M. Navon, and A. Mugeridge. Non-intrusive reduced order modelling of the Navier–Stokes equations. *Computer Methods in Applied Mechanics and Engineering*, 293:552–541, 2015.
- [29] D. Xiao, F. Fang, C. Pain, and G. Hu. Non-intrusive reduced order modelling of the Navier-Stokes equations based on RBF interpolation. *International Journal for Numerical Methods in Fluids*, 79(11):580–595, 2015.
- [30] Z Wang, D Xiao*, F Fang, R Govindan, CC Pain, and Y Guo. Model identification of reduced order fluid dynamics systems using deep learning. *International Journal for Numerical Methods in Fluids*, 2017.
- [31] D Xiao, F Fang, CC Pain, and IM Navon. A parameterized non-intrusive reduced order model and error analysis for general time-dependent nonlinear partial differential equations and its applications. *Computer Methods in Applied Mechanics and Engineering*, 317:868–889, 2017.
- [32] Z Lin, D Xiao, F Fang, CC Pain, and Ionel M Navon. Non-intrusive reduced order modelling with least squares fitting on a sparse grid. *International Journal for Numerical Methods in Fluids*, 83(3):291–306, 2017.
- [33] D Xiao, P Yang, F Fang, J Xiang, CC Pain, IM Navon, and M Chen. A non-intrusive reduced-order model for compressible fluid and fractured solid coupling and its application to blasting. *Journal of Computational Physics*, 330:221–244, 2017.
- [34] D Xiao, P Yang, F Fang, J Xiang, CC Pain, and IM Navon. Non-intrusive reduced order modeling of fluid-structure interactions. *Computer Methods in Applied Mechanics and Engineering*, 303:35–54, 2016.
- [35] D Xiao, F Fang, CC Pain, and IM Navon. Towards non-intrusive reduced order 3d free surface flow modelling. *Ocean Engineering*, 140:155–168, 2017.
- [36] Massimiliano Vasile, Edmondo Minisci, Domenico Quagliarella, Marc Guénot, Ingrid Lepot, Caroline Sainvitu, Jordan Goblet, and Rajan Filomeno Coelho. Adaptive sampling strategies for non-intrusive pod-based surrogates. *Engineering computations*, 30(4):521–547, 2013.

- [37] M Winter and C Breitsamter. *Reduced-Order Modeling of Unsteady Aerodynamic Loads Using Radial Basis Function Neural Networks*. Deutsche Gesellschaft für Luft-und Raumfahrt-Lilienthal-Oberth eV, 2014.
- [38] Chen Han. Blackbox stencil interpolation method for model reduction. Master’s thesis, Massachusetts Institute of Technology, 2012.
- [39] M Raisee, D Kumar, and C Lacor. A non-intrusive model reduction approach for polynomial chaos expansion using proper orthogonal decomposition. *International Journal for Numerical Methods in Engineering*, 2015.
- [40] H.Klie. Unlocking fast reservoir predictions via non-intrusive reduced order models. *The SPE Reservoir Simulation Symposium held in The Woodland, Texas, USA*, pages 1–16, 2013.
- [41] Edwin Insuasty, Paul MJ Van den Hof, Siep Weiland, and Jan Dirk Jansen. Tensor-based reduced order modeling in reservoir engineering: An application to production optimization. *IFAC-PapersOnLine*, 48(6):254–259, 2015.
- [42] D Xiao, Z Lin, F Fang, C C Pain, Ionel M Navon, P Salinas, and A Muggeridge. Non-intrusive reduced-order modeling for multiphase porous media flows using Smolyak sparse grids. *International Journal for Numerical Methods in Fluids*, 83(2):205–219, 2017.
- [43] Matthew Jackson, James Percival, Peyman Mostaghimi, Brendan Tollit, Dimitrios Pavlidis, Christopher Pain, Jefferson Gomes, Ahmed H Elsheikh, Pablo Salinas, Ann Muggeridge, et al. Reservoir modeling for flow simulation by use of surfaces, adaptive unstructured meshes, and an overlapping-control-volume finite-element method. *SPE Reservoir Evaluation & Engineering, SPE-163633-PA*, 18(02):115–132, 2015.
- [44] J.L.M.A. Gomes, D. Pavlidis, P. Salinas, Z. Xie, J.R. Percival, Y. Melnikova, C.C. Pain, and M. D. Jackson. A force-balanced control volume finite element method for multiphase porous media flow modelling. *Int. J. Numer. Meth. Fluids*, 83:431–445, 2017.
- [45] P. Salinas, D. Pavlidis, Z. Xie, C Jacquemyn, Y. Melnikova, C. C. Pain, and M. D. Jackson. Improving the robustness of the control volume finite element method with application to multiphase porous media flow. *International Journal for Numerical Methods in Fluids*, 85:235–246, 2017.
- [46] P.A. Forsyth. A control volume finite element approach to napl groundwater contamination. *SIAM Journal of Scientific and Statistical Computing*, 12:1029–1057, 1991.
- [47] L.J. Durlofsky. A triangle based mixed finite element finite volume technique for modelling two-phase flow through porous media. *Journal Computational Physics*, 105:252–266, 1993.
- [48] L.J. Durlofsky. Accuracy of mixed and control volume finite element approximations to Darcy velocity and related quantities. *Water Resources Research*, 30:965–973, 1994.

- [49] S. Geiger, S. Roberts, S.K. Matthai, C. Zoppou, and A. A. Burri. Combining finite element and finite volume methods for efficient multiphase flow simulations in highly heterogeneous and structurally complex geologic media. *Geofluids*, 4(4):284–299, 2004.
- [50] Z. Xie, D. Pavlidis, P. Salinas, J.R. Percival, C.C. Pain, and O.K. Matar. A balanced-force control volume finite element method for interfacial flows with surface tension using adaptive anisotropic unstructured meshes. *Computers and Fluids*, 138:38–50, 2016.
- [51] P. Salinas, D. Pavlidis, Z. Xie, A. Adam, C. C. Pain, and M. D. Jackson. Improving the convergence behaviour of a fixed-point-iteration solver for multiphase flow in porous media. *International Journal for Numerical Methods in Fluids*, 84(8):466 – 476, 2017.
- [52] Sergey A Smolyak. Quadrature and interpolation formulas for tensor products of certain classes of functions. 4(240-243):123, 1963.
- [53] P Salinas, D Pavlidis, Z Xie, A Adam, CC Pain, and MD Jackson. Improving the convergence behaviour of a fixed-point-iteration solver for multiphase flow in porous media. *International Journal for Numerical Methods in Fluids*, 84(8):466–476, 2017.
- [54] Y Melnikova, C Jacquemyn, H Osman, P Salinas, G Gorman, GJ Hampson, and MD Jackson. Reservoir modelling using parametric surfaces and dynamically adaptive fully unstructured grids. In *ECMOR XV-15th European Conference on the Mathematics of Oil Recovery*, 2016.
- [55] Pablo Salinas, Dimitrios Pavlidis, Zhihua Xie, Carl Jacquemyn, Yulia Melnikova, Matthew D Jackson, and Christopher C Pain. Improving the robustness of the control volume finite element method with application to multiphase porous media flow. *International Journal for Numerical Methods in Fluids*, 2017.
- [56] R Brooks and T Corey. HYDRAU uc Properties Of Porous Media. *Hydrology Papers, Colorado State University*, 1964.